

Euclid: Disky titans – surprisingly high star formation efficiency in two brightest group galaxies at $z \sim 0.75$ ★

F. Gentile^{★,★1,2}, E. Daddi³, D. Elbaz³, A. Enia², F. Vito², P.-A. Duc⁴, M. Franco³, H. Fu^{5,6}, R. Giuffrida³, D. Roberts⁶, F. Shankar⁶, S. Lu^{7,8,9}, P. Awad¹⁰, J.-B. Billand¹, M. Baes¹¹, L. Bisigello¹², E. Duran-Camacho^{13,14}, G. Castignani², O. Cucciati², G. De Lucia¹⁵, C. D’Eugenio^{16,1}, D. Donevski^{17,18}, M. Fossati^{19,20}, M. Fumagalli^{19,15}, R. Gobat²¹, C. Gruppioni², M. Magliocchetti²², B. Magnelli³, G. Papini^{2,23}, L. Pozzetti², V. Sangalli³, J. G. Sorce^{24,25}, L. Spinoglio²², V. Strazzullo^{15,26}, M. Tarrasse¹, G. Toni^{23,2,27}, G. Zamorani², B. Altieri²⁸, S. Andreon²⁰, N. Auricchio², C. Baccigalupi^{26,15,29,17}, M. Baldi^{30,2,31}, S. Bardelli², P. Battaglia², A. Biviano^{15,26}, E. Branchini^{32,33,20}, M. Brescia^{34,35}, S. Camera^{36,37,38}, V. Capobianco³⁸, C. Carbone³⁹, J. Carretero^{40,41}, M. Castellano⁴², S. Cavuoti^{35,43}, A. Cimatti⁴⁴, C. Colodro-Conde¹³, G. Congedo⁴⁵, L. Conversi^{46,28}, Y. Copin⁴⁷, F. Courbin^{48,49,50}, H. M. Courtois⁵¹, M. Cropper⁵², H. Degaudenzi⁵³, H. Dole²⁵, F. Dubath⁵³, X. Dupac²⁸, M. Farina²², R. Farinelli², F. Faustini^{42,54}, S. Ferriol⁴⁷, S. Fotopoulou⁵⁵, M. Frailis¹⁵, E. Franceschi², M. Fumana³⁹, S. Galeotta¹⁵, K. George⁵⁶, B. Gillis⁴⁵, C. Giocoli^{2,31}, J. Gracia-Carpio⁵⁷, A. Grazian¹², F. Grupp^{57,58}, S. Gwyn⁵⁹, S. V. H. Haugan⁶⁰, H. Hoekstra¹⁰, W. Holmes⁶¹, I. M. Hook⁶², F. Hormuth⁶³, A. Hornstrup^{64,65}, K. Jahnke⁶⁶, M. Jhabvala⁶⁷, B. Joachimi⁶⁸, S. Kermiche⁶⁹, A. Kiessling⁶¹, B. Kubik⁴⁷, M. Kümmel⁵⁸, M. Kunz⁷⁰, H. Kurki-Suonio^{71,72}, A. M. C. Le Brun⁷³, S. Ligi³⁸, P. B. Lilje⁶⁰, V. Lindholm^{71,72}, I. Lloro⁷⁴, G. Mainetti⁷⁵, O. Mansutti¹⁵, O. Marggraf⁷⁶, M. Martinelli^{42,77}, N. Martinet⁷⁸, F. Marulli^{23,2,31}, R. J. Massey⁷⁹, E. Medinaceli², S. Mei^{80,81}, M. Melchior⁸², M. Meneghetti^{2,31}, E. Merlin⁴², G. Meylan⁸³, A. Mora⁸⁴, M. Moresco^{23,2}, L. Moscardini^{23,2,31}, R. Nakajima⁷⁶, C. Neissner^{85,41}, S.-M. Niemi⁸⁶, C. Padilla⁸⁵, S. Paltani⁵³, F. Pasian¹⁵, K. Pedersen⁸⁷, W. J. Percival^{88,89,90}, V. Pettorino⁸⁶, G. Polenta⁵⁴, M. Poncet⁹¹, L. A. Popa⁹², F. Raison⁵⁷, A. Renzi^{93,94,2}, J. Rhodes⁶¹, G. Riccio³⁵, E. Romelli¹⁵, M. Roncarelli², H. J. A. Rottgering¹⁰, B. Rusholme⁹⁵, R. Saglia^{58,57}, Z. Sakr^{96,97,98}, D. Sapone⁹⁹, P. Schneider⁷⁶, T. Schrabback¹⁰⁰, A. Secroun⁶⁹, E. Sihvola¹⁰¹, P. Simon⁷⁶, C. Sirignano^{93,94}, G. Sirri³¹, J. Skottfelt¹⁰², L. Stanco⁹⁴, P. Tallada-Crespi^{40,41}, A. N. Taylor⁴⁵, H. I. Teplitz¹⁰³, I. Tereno^{104,105}, S. Toft^{106,107}, R. Toledo-Moreo^{108,109}, F. Torradeflot^{41,40}, I. Tutusaus^{110,111,97}, J. Valiviita^{71,72}, T. Vassallo^{15,56}, G. Verdoes Kleijn¹¹², A. Veropalumbo^{20,33,32}, Y. Wang⁹⁵, J. Weller^{58,57}, F. M. Zerbi²⁰, E. Zucca², M. Bolzonella², M. Huertas-Company^{13,113,114}, and M. Sereno^{2,31}

(Affiliations can be found after the references)

2026-06-03

ABSTRACT

We present the discovery of two diskly titans in the first data release of the *Euclid* satellite. These sources are massive ($M_* > 10^{11} M_\odot$) star-forming (SFR $\sim 20 M_\odot \text{ yr}^{-1}$) discs located in strong over-densities at intermediate redshift ($z \sim 0.75$). They represent a small fraction of the massive galaxies in over-dense regions (just four candidates in more than 20 deg^2 analysed in this study), and their existence is puzzling considering the abundance of passive and bulge-dominated sources commonly found at the centre of groups and clusters at low redshift. Firstly, our analysis shows that these objects are located in massive groups ($M_h \sim 10^{13.8} M_\odot$), where rapid accretion of cold gas should be prevented from the formation of a static hot halo. Despite this, a millimetre follow-up with NOEMA shows significant cold gas reservoirs ($M_{\text{H}_2} \sim 10^{10.3} M_\odot$) within these sources. Secondly, our morphological analysis shows the presence of a massive and passive bulge in these galaxies, which is expected to stabilise the disc against fragmentation thereby suppressing further star formation. However, these sources lie on the Schmidt–Kennicutt relation or even slightly above. Building on these observations, we propose a scenario where these diskly titans are the product of a merger-induced rejuvenation episode, in which the most massive galaxy of a group accretes cold gas from another member and briefly restarts star-formation. Such scenario is supported by a comparison with the TNG300 simulation and easily explains the surviving of star-formation activity in massive galaxies in over-dense environments as temporary stages in a more complex evolution. More in general, our study showcases the ability of *Euclid* to find rare objects thanks to the unprecedented statistics offered by its surveys and the scientific potential residing in the synergy between *Euclid* and other facilities observing at longer wavelengths.

1. Introduction

One of the main observational results in extragalactic astronomy is the existence of a strong bimodality between star-forming and quiescent galaxies (e.g., [Kauffmann et al. 2003](#); [Brinch-](#)

[mann et al. 2004](#)). The first population is composed by objects with blue rest-frame colours, high star-formation activity, and younger stellar ages, while the second includes galaxies with redder colours, lower star-formation rates (SFRs), and hosting older stellar populations. Quite remarkably, this distinction is found to extend to other physical properties such as morphologies (with red objects being bulge-dominated, while blue sources

★ This paper is published on behalf of the Euclid Consortium.

** e-mail: fabrizio.gentile@cea.fr

tend to present more dominant disk structures – see, e.g., Wuyts et al. 2011; Euclid Collaboration: Quilley et al. 2025 – even though some notable exceptions are known, see, e.g. Masters et al. 2010; McIntosh et al. 2014). The existence of this bimodality is commonly interpreted as evidence that two main processes must be in place during the evolution of galaxies: galaxy quenching and morphological transformation. Quenching causes the strong suppression of the star-formation activity, while the other is related to the transition from a disc-dominated morphology into a bulge-dominated one. Moreover, the small number of galaxies found in between these two main populations is commonly interpreted as the evidence that both phenomena take place on a timescale much shorter than the total amount of time spent by galaxies as star-forming or passive. Despite the decades spent by the community studying this problem, a clear picture of these two phenomena, their interplay, and the physical mechanisms responsible for them, is still missing.

From an observational point of view, both phenomena are found to be tightly related to the galaxy stellar mass (with the fraction of passive and spheroidal objects – in a given environment – constantly found to be higher at higher masses; see, e.g., Pozzetti et al. 2010; Shuntov et al. 2025), and to their local environment (the same fractions are found to increase in more dense environments at fixed stellar mass; see, e.g., Dressler 1980; Bolzonella et al. 2010; Peng et al. 2010; Euclid Collaboration: Cleland et al. 2025; Euclid Collaboration: Gentile et al. 2025). For this reason, we commonly introduce two large families of processes called, respectively, mass- and environmental-quenching (see, e.g., Peng et al. 2010). The mass-quenching group includes all internal processes that are commonly related to higher stellar masses, such as feedback from active galactic nuclei (AGN; e.g., Bower et al. 2006; Croton et al. 2006) or morphological quenching (Martig et al. 2009, 2013) in which a massive and passive bulge (more common in massive galaxies) stabilises the stellar disc preventing star-formation. The other group includes external mechanisms that are thought to be more efficient in dense environments either by preventing the accretion of cold gas onto galaxies (e.g., through halo shock heating or starvation, mostly affecting high-mass sources; Dekel & Birnboim 2006; van den Bosch et al. 2008) or by taking it away (e.g., through tidal stripping or ram-pressure stripping, more effective in low-mass objects; Gunn & Gott 1972; Feldmann et al. 2010; Boselli et al. 2022). Both families of processes are then expected to show their maximum efficiency in the massive galaxies located at the centre of over-dense regions (normally called brightest group or cluster galaxies – BGGs or BCGs – depending on the size of the structure hosting them). Indeed, these sources are found – in the vast majority of cases – to be passive and spheroidal galaxies, at least up to $z \sim 1$ (e.g., López-Cruz et al. 2004; Whiley et al. 2008; Fraser-McKelvie et al. 2014), even though rare exceptions have been discovered and well studied in the past decade (see, e.g., Fogarty et al. 2015, 2019; Castignani et al. 2020, 2022, 2023).

The overall scenario characterised by the interplay between mass- and environmental-quenching outlined above has been confirmed in the last decade by several observational studies and simulations (e.g., Peng et al. 2010; Bahé et al. 2017; Henriques et al. 2017; Weller et al. 2025; Ghaffari et al. 2026). In the last year, in particular, the launch of the *Euclid* space telescope gave us access to an unprecedented statistic of galaxies with a reliable estimation of their physical properties and morphologies coupled with a well-characterised environment. These new possibilities already allowed us to confirm the overall correlation between properties, morphologies, mass, and environment (Euclid Collaboration: Cleland et al. 2025), as well as separate the study of

quenching and morphological transformation, and analyse their interplay (Euclid Collaboration: Gentile et al. 2025).

In this paper, we focus on another main asset of *Euclid*: the ability to find rare objects. The large statistic is thus indeed crucial to find outliers of well-assessed relations, giving us the opportunity to investigate in detail cases in which the processes that are thought to be responsible for the observed trends seem less efficient or not at play at all. More in detail, in this paper we present the discovery of two “disky titans”. These rare sources (just four in over 20 deg^2 covered by the *Euclid* telescope in the first data released by the collaboration) are defined as massive ($M_* > 10^{11} M_\odot$), disk galaxies found to be star-forming ($\text{SFR} \gtrsim 20 M_\odot \text{ yr}^{-1}$) even if located in strong over-densities.

This paper focuses on the characterisation of a first (pilot) sample of two sources, for which millimetre (mm) data obtained from the Northern Extended Millimetre Array (NOEMA) are available. The main goal of this study is to constrain their physical properties, characterise their environment, model their morphology, and offer a likely scenario explaining their observed properties.

This paper has the following structure. In Sect. 2 we present the multi-wavelength data on which our analysis is based. Section 3 focuses on the characterisation of the two galaxies in terms of gas content, physical properties, and morphology. In Sect. 4, we characterise the two groups in which the two galaxies are located and estimate their halo mass. In Sect. 5 we discuss our findings, propose a likely scenario able to explain our observations, and verify its plausibility by looking for analogue sources in hydrodynamical simulations. Finally, we draw our conclusions in Sect. 6 and forecast the possible future perspective of this work.

Throughout this study, we assume a standard Λ CDM cosmology with the parameters reported in Planck Collaboration: Aghanim et al. (2020). We also assume the initial mass function by Chabrier (2003). Finally, all the magnitudes quoted throughout the text are reported in the AB photometric system (Oke & Gunn 1983).

2. Data and target selection

2.1. *Euclid* data

The space-based imaging and photometry analysed in this paper come from the first Data Release (DR1; Euclid Collaboration: Aussel et al., *in prep.*) of the *Euclid* telescope. These data include a first small fraction (about 1900 deg^2) of the Euclid Wide Survey (EWS; Euclid Collaboration: Scaramella et al. 2022) and deeper observations of the Euclid Deep Fields (EDFs; about 53 deg^2) already included in the first Quick Data Release (Euclid Quick Release Q1 2025; Euclid Collaboration: Aussel et al. 2025). Unlike Q1 data, DR1 includes several visits covering two of the EDFs (Euclid Deep Field North and South, EDF-N and EDF-S, respectively) to reach higher depths.

Euclid provides space-based imaging in four filters: one large optical band (I_E , Euclid Collaboration: Cropper et al. 2025) and three near-infrared ones (Y_E , J_E , and H_E ; Euclid Collaboration: Jahnke et al. 2025). The two targets presented in this paper are located in the EDF-N (about 22.9 deg^2 ; Euclid Collaboration: Aussel et al., *in prep.*). Hence, they are covered by ten passes of the telescope released in DR1, ensuring a 5σ depth in $2''$ apertures of 26.5, 24.9, 25.1, and 25.0 in I_E , Y_E , J_E , and H_E , respectively (about 1 magnitude deeper than Q1 data; see Euclid Collaboration: Romelli et al. 2025).

These space-based data are complemented by ground-based observations collected as part of the Ultraviolet Near Infrared

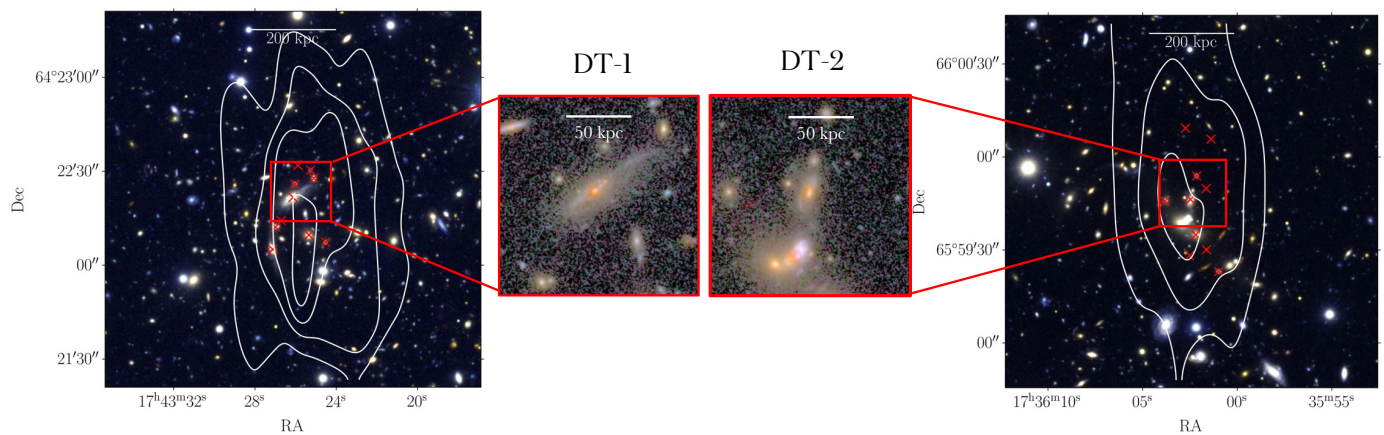


Fig. 1. Colour-composite images of the two targets analysed in this paper and the surrounding environments. Each large image covers one square arcminute, with a side roughly corresponding to 441 proper kpc at $z \sim 0.7$ and it is obtained through the Lupton et al. (2001) algorithm by combining the I_E , Y_E , and H_E images. The white curves are the galaxy density field in units of σ above the median starting from 3σ . The candidate members (i.e., with a redshift compatible with the over-density and with a density contrast higher than 3σ) are marked with red crosses. The inner panels report a zoom on the two diskly titans, with sides of $20'' \times 20''$. These images are generated with Jafar¹ to highlight low surface brightness features by combining the four *Euclid* bands.

Optical Northern Survey (UNIONS; Gwyn et al. 2025), granting ancillary data in the five *ugriz* bands by combining different surveys observing the northern hemisphere, with depths spanning the range 23.1 – 24.9 mag. More details on the specific surveys used for ground-based ancillary photometry can be found in Euclid Collaboration: Mellier et al. (2025) and in Gwyn et al. (2025).

Photometry is extracted in all bands through the MER pipeline (responsible for the assembly of the photometric catalogues from the *Euclid* observations and from the external data; see Euclid Collaboration: Kümmel et al., *in prep.*) and passed to the PHZ pipeline (Euclid Collaboration: Hartley et al., *in prep.*; Euclid Collaboration: Enia et al., *in prep.*) in which photometric redshifts and physical properties are then derived with the machine-learning algorithm Nearest-Neighbour Photometric Redshift (nnpz; Euclid Collaboration: Desprez et al. 2020; Euclid Collaboration: Enia et al. 2024).

These measurements are used to compute a mass completeness limit for our data. Following the standard procedure by Pozzetti et al. (2010) applied to passive galaxies (colour-selected in the rest-frame $NUV - r$, $r - J$ plane, see Ilbert et al. 2010) brighter than $H_E < 25$, we obtain that the *Euclid* deep survey in the EDF-N is 90% mass-complete for masses higher than $M_{\text{lim}} = 10^9 M_\odot$ at $z \sim 0.8$. Since one of our targets is located in the fraction of EDF-N covered by *Spitzer* observations as part of the Cosmic Dawn Survey (Euclid Collaboration: Moneti et al. 2022; Euclid Collaboration: McPartland et al. 2025), we complement the *Euclid* and external photometry with that provided by the Infrared Array Camera (IRAC), as extracted by Euclid Collaboration: Bisigello et al. (2025).

2.2. Target selection

The targets analysed in this paper are selected starting from the density maps built by Euclid Collaboration: Gentile et al. (2025). In this study, the authors employed the first Q1 data from *Euclid* to model the density fields of the three EDFs in the redshift range $0.25 < z < 1$. Starting from their catalogue of the EDF-N (accessible with ground-based facilities observing in the northern sky and covered by deeper *Euclid* DR1 data), we firstly select galax-

ies belonging to strong over-densities, for example with a density contrast parameter $\log_{10}(1 + \delta)$ above 5σ from the median at their redshift, and then – to reduce the contamination by satellite galaxies – we further select galaxies with $M_* > 10^{11} M_\odot$. Following these criteria, we obtain a sample of 42 likely BGGs or BCGs. From this parent sample, we select star-forming galaxies based on their $NUV - r$ and $r - J$ colours (Ilbert et al. 2010) and on their distance from the main sequence of star-forming galaxies (MS; Euclid Collaboration: Enia et al. 2025) being lower than the intrinsic scatter of the relation ($\sigma \sim 0.3$ dex). This additional step leaves us with a sample of four star-forming BCG or BGG candidates in the EDF-N. The two final candidate diskly titans (hereafter dubbed DT-1 and DT-2) were selected based on the clearer presence of a stellar disc and of a narrower redshift probability function ($z_{\text{phot},1} = 0.69 \pm 0.05$ and $z_{\text{phot},2} = 0.78 \pm 0.01$, respectively). Colour-composite images of the two targets discussed in this paper and of the surrounding environments are shown in Fig. 1.

2.3. NOEMA Data

The millimetre data for the two objects analysed in this paper come from the NOEMA program S25BT (P.I.: F. Gentile). These data consist of interferometric observations at $\lambda \sim 2$ mm having the main goal of observing the CO(2-1) line at $z \sim 0.7$. The large bandwidth offered by the NOEMA interferometer is crucial to identify the targeted line when only photometric redshifts are available. The data were collected with the interferometer in its most compact configuration (D), ensuring a clean beam of $3''.3 \times 2''.8$ at the declination of our targets. Each target was observed for a total of eight hours, allowing us to achieve a noise level of $130 \mu\text{Jy beam}^{-1}$ when integrated over 500 km s^{-1} , slightly variable with frequency.

The data are reduced with the GILDAS code suite (version sep25a; Gildas Team 2013) by employing the standard NOEMA pipeline. The reduced data are composed of two data cubes, centred on the two targets, covering two spectral win-

¹ <https://jafar.astro.unistra.fr/>

dows of nearly 8 GHz each in the range 134–142/149–157 and 127–135/142–150 GHz for the two objects, respectively.

2.4. X-ray data for DT-2

DT-2 was serendipitously observed by the X-ray Multi-Mirror Mission (XMM-Newton) telescope, as part of the program 0202100301 (P.I.: A. Wolter). The observations targeted the AGN NEP 2131 (Wolter et al. 2005), located around 7 arcmin away from DT-2, with an exposure time of 37 409 s. It is interesting to notice how the structure hosting DT-2 was already listed as a possible cluster of galaxies by Mehrrens et al. (2012) due to its extended X-ray emission in the soft band. Unfortunately, the lack of deep optical observations before *Euclid* made it impossible to perform a complete analysis of this object. We download the raw X-ray data from the XMM archive² and perform the reduction. We employ the Science Analysis System (SAS v21.1³) – a suite of libraries especially designed to reduce and analyse data collected by XMM – for data reduction, image creation, and spectral extraction, following standard procedures. In summary, we first use the `eprocc` and `emproc` tools to concatenate and calibrate the event lists. Then, we employ `evselect` to create light-curves in the 10–12 keV and > 10 keV energy bands for the PN and MOS instruments, respectively. We filter out background flaring periods with count rates > 0.4, 0.15, and 0.25 cts s⁻¹ for the PN, MOS1, and MOS2 cameras, respectively, resulting in clear exposure times of 18.0, 21.7, 21.6 ks. Finally, we use the `evselect`, `eexmap`, `backscale`, `rmfgen`, and `arfgen` tools to create images and exposure maps and to extract spectra, response matrices, and ancillary files. These data will be used in Sect. 4.2 to constrain the halo mass of the structure hosting DT-2. No observations covering DT-1 are found in the archive.

3. Characterisation of the galaxies

3.1. Spec-z and gas mass

The analysis of the two data cubes produced by NOEMA is performed with the Common Astronomy Software Applications (CASA 6.7.2; CASA Team et al. 2022) package. We follow the procedure described in Jin et al. (2019) and Gentile et al. (2024) to blindly search for emission line in our data. Firstly, we extract a spectrum at the expected position of our targets based on the high-resolution images provided by *Euclid*. The extraction is performed in the visibility space with an elliptical Gaussian model with shape parameters obtained by fitting the model to the 0-moment of the CO emission. The extracted spectrum is then convolved with a series of boxcar filters with different widths, each time looking at the signal-to-noise ratio (S/N) of the brightest peak of emission. This procedure allows us to detect a bright line in each spectrum, with observed frequencies of $\nu_1 = (135.69 \pm 0.02)$ GHz and $\nu_2 = (130.45 \pm 0.01)$ GHz for DT-1 and DT-2⁴, respectively, and an S/N of 5.2 and 9.1. Following the procedure described in Jin et al. (2019), we estimated a spurious probability of 10^{-3} and 10^{-6} for the two lines, sufficient to ensure the reliability of our detections. Once masked the two detected lines, we are also able to detect a continuum signal by

Table 1. Main properties estimated for the two diskly titans presented in this paper.

	DT-1	DT-2
RA	17 ^h 43 ^m 26 ^s .17	17 ^h 36 ^m 2 ^s .45
Dec	64° 22′ 21″.50	65° 59′ 46″.05
z_{spec}	0.6990 ± 0.0002	0.7672 ± 0.0001
$\log_{10}(M_*/M_{\odot})$	11.30 ± 0.05	11.25 ± 0.08
$\log_{10}(\text{SFR}_{\text{SED}}/M_{\odot} \text{ yr}^{-1})$	1.4 ± 0.2	1.4 ± 0.2
$\log_{10}(\text{SFR}_{\text{IR}}/M_{\odot} \text{ yr}^{-1})$	1.3 ± 0.1	1.6 ± 0.1
A_v [mag]	2.1 ± 0.6	1.9 ± 0.8
$r_{\text{phys}}(I_E)$ [kpc]	21.7 ± 0.3	13.5 ± 0.1
$r_{\text{phys}}(H_2)$ [kpc]	35 ± 5	25 ± 2
$I_{\text{CO}(2-1)}$ [Jy km s ⁻¹]	0.8 ± 0.1	0.83 ± 0.09
Width [km s ⁻¹]	442	689
$\log_{10}(M_{H_2}/M_{\odot})$	10.3 ± 0.1	10.4 ± 0.1
μ_{H_2}	0.10 ± 0.02	0.14 ± 0.04
τ_{dep} [Myr]	794 ± 375	1000 ± 690
$S_{2\text{mm}}$ [μJy]	42 ± 15	86 ± 24
$\log_{10}(M_{\text{Dust}}/M_{\odot})$	8.0 ± 0.3	8.3 ± 0.2
$\log_{10}(M_{\text{Dust}}/M_*)$	-3.3 ± 0.4	-3.0 ± 0.3

Notes. The spectroscopic redshift of the galaxies is derived from the CO(2-1) transition observed with NOEMA, as well as the information about the gas content (Sect. 3.1). The constraints on the dust content come from the continuum emission, while the other physical properties are measured through SED fitting with CIGALE (Sect. 3.3).

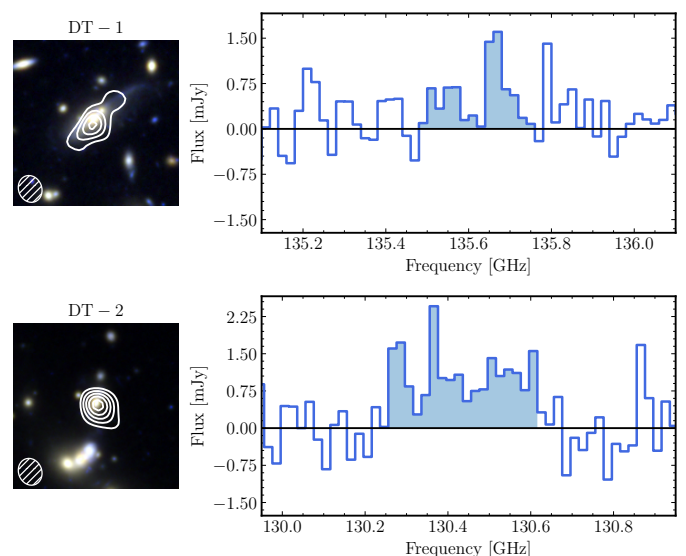


Fig. 2. Two CO(2-1) lines observed with NOEMA in the two targets presented in this paper. For each galaxy, the right panel reports their millimetre spectrum, with the channels belonging to the line (i.e., maximising its S/N; see Sect. 2.3) coloured in blue. The left panels show the moment-0 of the line superimposed to the color-composite image of the target. Contours increase by 1σ , starting from 2σ and 5σ for the two galaxies, respectively. The synthesised beam is shown in the bottom left corner for reference.

stacking the remaining channels, obtaining two marginal detections with S/N of 2.8 and 3.6, respectively. The observed lines, together with their 0-moments are shown in Fig. 2. Even though the resolution does not allow for a complete dynamical model of the two lines, it is possible to notice how both present a double-peaked profile, a typical hint of rotation in the gas phase of our

² <https://nxs.esac.esa.int/nxs-web/#search>

³ <https://www.cosmos.esa.int/web/xmm-newton/download-and-install-sas>

⁴ The uncertainties are computed by fitting a Gaussian function to the spectrum through a Monte Carlo Markov Chain implemented with the `emcee` library (Foreman-Mackey et al. 2013).

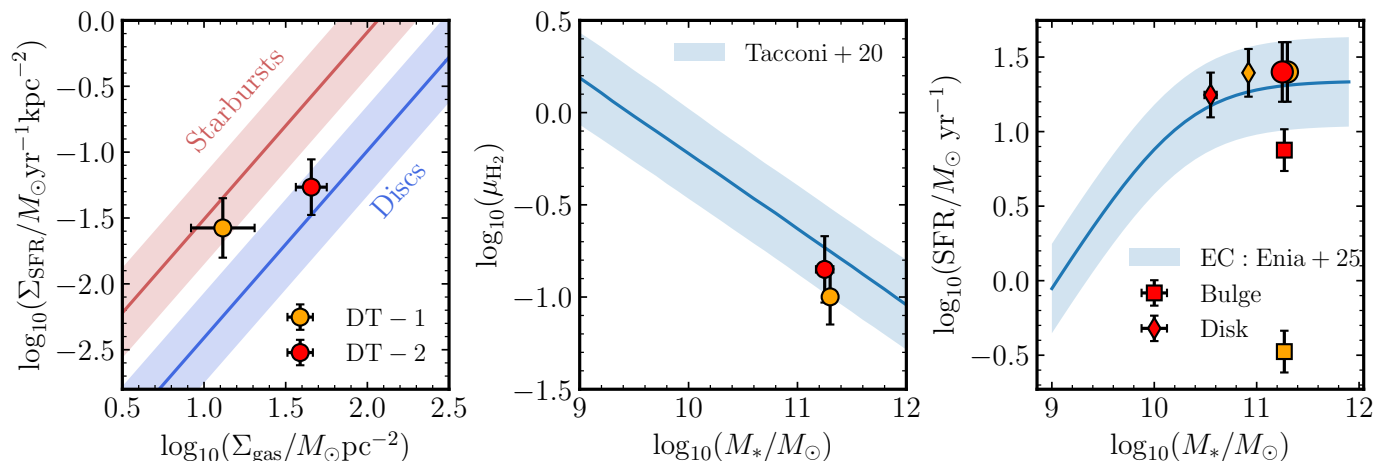


Fig. 3. Two disk galaxies compared with the Schmidt–Kennicutt relation (Schmidt 1959; Kennicutt 1998; *left panel*), with the main sequence of star-forming galaxies (as parametrised by Euclid Collaboration: Enia et al. 2025; *right panel*), and with the molecular gas fraction expected for MS galaxies at $z \sim 0.75$ (Tacconi et al. 2020; *central panel*). In the *left panel*, we report the sequence of discs and star-bursting galaxies following Daddi et al. (2010b). In the *right panel*, we report the masses and SFR integrated over the whole galaxies, and of their bulges and disks separately (squares and diamonds, respectively) derived following the procedure described in Sect. 3.2–3.3.

galaxies (which is expected, given the disk shape of the stellar component).

The integrated flux ($I_{\text{CO}(2-1)}$) and the widths of the detected lines (i.e., the range of channels maximising the S/N), together with the detected continua ($S_{2\text{mm}}$) are reported in Table 1. Given the photometric redshifts of the two sources (Sect. 2.2), we model the two lines as CO(2-1) transition ($\nu_0 = 230.538$ GHz), translating into spectroscopic redshifts of $z_1 = 0.6990 \pm 0.0002$ and $z_2 = 0.7672 \pm 0.0001$, respectively. We underline that alternative modellings for the detected lines, albeit possible, would yield redshifts in strong tension with the observed photometry of the two targets.

Moreover, since the low rotational transitions of the CO molecule are well-known tracers of molecular gas (see, e.g., the review by Bolatto et al. 2013 and references therein), we employ the detected lines to estimate the gas mass of our targets. Firstly, we rescale the measured CO(2-1) fluxes of the two targets into that expected for CO(1-0), by assuming a standard ratio $R_{21} = 0.64 \pm 0.09$ commonly employed for star-forming galaxies (den Brok et al. 2021, see also another compatible estimation in Daddi et al. 2015). Then, we convert the CO(1-0) luminosity into a gas mass through the standard relation (e.g., Bolatto et al. 2013)

$$M_{\text{H}_2} = 3.25 \times 10^7 \alpha_{\text{CO}} I_{\text{CO}(1-0)} \nu_{\text{obs}}^{-2} D_L^2 (1+z)^{-3}, \quad (1)$$

where D_L is the luminosity distance. Since, according to the selection scheme, the two targets are located in the MS (see Sect. 2.2), we adopt a standard value of $\alpha_{\text{CO}} = (3.6 \pm 0.8) M_\odot \text{pc}^{-2} (\text{K km s}^{-1})^{-1}$, as commonly done for these kinds of sources (Daddi et al. 2010b,a). The estimated molecular gas masses, together with the gas fractions ($\mu_{\text{H}_2} = M_{\text{H}_2}/M_*$) and the depletion times ($\tau_{\text{dep}} = M_{\text{H}_2}/\text{SFR}$) are reported in Table 1. We underline that the choice of a lower value of α_{CO} would produce lower values of the gas mass and depletion time. For instance, a starburst value of $\alpha_{\text{CO}} \sim 0.8 M_\odot \text{pc}^{-2} (\text{K km s}^{-1})^{-1}$ (e.g., Bolatto et al. 2013) would produce a gas mass 4.5 times lower. The choice of such value, however, is not supported by the observed value of SFR (see Sect. 3.3).

In the central panel of Fig. 3, we compare the obtained molecular gas fraction with those expected for MS galaxies (Tacconi et al. 2020) with the same mass at a reference redshift of

$z = 0.75$. We show that both estimates are compatible – within the uncertainties – with the expectations. Similarly, in the left panel of Fig. 3, we compare the surface density of molecular gas and of SFR with the relation by Schmidt (1959) and Kennicutt (1998) normally holding for star-forming galaxies. For doing this, we divide the two quantities by a reference surface chosen as that of the CO emission and of the I_E emission for the molecular gas and SFR, respectively. We show that DT-2 lies – within the uncertainties – on the relation, while DT-1 is located above, indicating a lower depletion time and, consequently, a higher star-formation efficiency ($\text{SFE} \sim \tau_{\text{dep}}^{-1}$), compatible with the expectations for star-bursting galaxies (Daddi et al. 2010b). These results will be discussed in Sect. 5 to explain the observed properties of our two disk galaxies.

3.2. Morphological analysis

We perform a morphological analysis of our two targets by fitting two Sérsic profiles to their images at different wavelengths. Each combined model has in principle 12 free parameters, but we impose the equality between the centres of the two profiles and fix the Sérsic index of the disk component to one, reducing to nine the number of parameters to be fitted. The combined model is then fitted to the four high-resolution images (I_E , Y_E , J_E , and H_E) separately. We find that the bulge-to-total luminosity ratio is strongly dependent on the wavelength, increasing from 0.2 and 0.3 in the I_E band to 0.5 and 0.9 in H_E for the two targets, respectively. In addition, both bulge components of the two galaxies in the NIR bands have a high Sérsic index ($n_{\text{bulge}} \sim 6$), compatible with a velocity-dispersion-dominated structure (Kormendy & Kennicutt 2004; Fisher & Drory 2008). Figure 4 shows the results of our modelling procedure. From the same figure (see also Fig. 1) it is also possible to notice that both targets present some irregularities in their brightness profile: a significant tidal tail is visible in both sources, with a stronger feature being present in DT-1. Similarly, a clumpy structure is visible in the residuals of DT-1, with three components detected in I_E and a single one visible in H_E . The presence of these features will be used in Sect. 5 to constrain our evolutionary scenario for these sources.

As a final step, in order to reconstruct the total SED of the two morphological components for our objects, we extend the complete analysis to the ground-based bands. Given the lower spatial resolution of these data, we fix the value of all the parameters in the double Sérsic profile to those obtained on the I_e band (i.e., that with the highest wavelength overlap with those bands) with the only exception of the normalisation. The obtained fluxes will be employed in Sect. 3.3 to estimate the physical properties of the two components of our galaxies.

3.3. SED fitting

To complement the physical properties estimated with the `nnpz` algorithm implemented in the *Euclid* pipeline, we perform a traditional SED-fitting with CIGALE (Boquien et al. 2019). The chosen setup includes the single stellar population models by Bruzual & Charlot (2003), combined through a delayed exponentially declining star-formation history. Dust attenuation is taken into account following the model by Charlot & Fall (2000), while nebular emission is included with the set of Cloudy models (Ferland et al. 1998) realised by Inoue (2011). The photometry given as input to CIGALE is the one described in Sect. 2.1 and provided by the *Euclid* MER pipeline⁵ for the two galaxies considered as a whole, with the addition of an IRAC data-point at $\lambda = 3.6\ \mu\text{m}$ for DT-2 (see Sect. 2.1). For the bulge and disk-components of the two objects, we employ the photometry obtained through the procedure outlined in Sect. 3.2. In this case, the uncertainties are the sum in quadrature of the photometric uncertainties and of those related to the modelling procedure. The results of our SED-fitting procedure are shown in Fig. 5.

Looking at the results for the galaxies when considered in their integrity (Fig. 3 and Table 1), we notice how the sources are located in the high-mass end of the MS (according to the parametrisation by Euclid Collaboration: Enia et al. 2025). The high precision on the estimate of the stellar masses for the two objects is driven by the photometric coverage of the rest-frame NIR wavelengths granted by the H_e filter (and the first channel of IRAC for DT-2). At the same time, SFR of the two sources has larger uncertainties, mostly due to the lack of photometric constraints on the rest-frame UV regime. An alternative estimation of the SFR for these sources comes from the measured continuum fluxes at $\lambda \sim 2\ \text{mm}$ (Sect. 3.1). We convert these quantities into infrared luminosities through the standard templates for star-forming galaxies by Schreiber et al. (2018). These quantities are then converted into SFRs by using the standard relation by Kennicutt & Evans (2012). The inferred values are reported in Table 1 and are compatible – within the estimated uncertainties – with those derived from SED-fitting. We underline that these values for the SFR are derived using the hypothesis that no significant AGN contribution is visible in the UV or at longer wavelengths. The assumption of no AGN contribution is based on the lack of X-ray detections for DT-2 (Fig. 6) and radio detections at 150 MHz in the LOFAR maps covering the EDF-N (Bondi et al. 2024; Bisigello et al. 2025) for both galaxies. Regarding the X-rays, we perform a simple test with the software PIMMS⁶ to compute the expected X-ray flux of an AGN in our data. By assuming a low-luminosity AGN of $L_x \sim 10^{42.5}\ \text{erg s}^{-1}$,

⁵ For consistency with `nnpz`, we use the photometry extracted in fixed circular apertures with a radius equal to twice the point spread function full width at half maximum in the u band with a wavelength-dependent aperture correction to account for the missing flux.

⁶ <https://heasarc.gsfc.nasa.gov/cgi-bin/Tools/w3pimms/w3pimms.pl>

with standard values $n_H = 10^{22}\ \text{cm}^{-2}$ (hydrogen column density) and $\Gamma = 1.7$ (index of the power-law spectrum), we obtain a total count of about eight photons in the energy range 0.5–2 keV, below the detection limit of our observations. Therefore, a low-luminosity AGN cannot be excluded in ID-2 (and similarly in ID-1, due to the lack of X-ray coverage). However, we note that the presence of nuclear activity in our galaxies would not affect the two main quantities involved in our analysis: the SFR and the gas mass. The first one could be affected if the rest-UV emission had a contribution from the accretion disc of the AGN, but the availability of a second tracer in the mm allows us to reject such possibility.

From the differential analysis of the two morphological components, we see that the star-formation activity of the two galaxies is almost completely concentrated in the stellar disc, which contains 98% and 70% of the total SFR for the two galaxies, respectively. Similarly, the stellar mass is mostly confined to the bulges, accounting for 70% and 84% of the total stellar mass.

Moreover, additional information on the stellar populations hosted in our targets can be derived from the best-fitting SEDs. At the redshift of our objects ($z \sim 0.75$), the observed wavelength of the Balmer break falls between the r and i filters, making the $i - r$ colour a good estimator of the strength of the break. For this reason, we expect to have good constraints on the age of the main stellar population within the two galaxies from the SED-fitting, even in the absence of rest-optical spectroscopy in the region of the break. For both galaxies, the SED-fitting procedure shows that the bulge is significantly older than the disc, with stellar ages on the order of about 5 Gyr, while the same quantities for the discs are on the order of 1 Gyr.

Finally, the same constraints on the continuum emission at $\lambda \sim 2\ \text{mm}$ can be used to measure the gas mass within our targets. Given that our observations sample the rest-frame $\lambda \sim 1\ \text{mm}$ wavelength (on the Rayleigh–Jeans tail of the thermal dust emission), we can employ the observed fluxes to estimate the gas mass. This conversion is carried out through the same templates by Schreiber et al. (2018), yielding dust masses on the order of $M_{\text{Dust}} \sim 10^{8-8.3}\ M_\odot$ (see Table 1). These quantities can then be converted into dust-to-stellar mass ratios of $\log_{10}(M_{\text{Dust},1}/M_{*,1}) = -3.3 \pm 0.4$ and $\log_{10}(M_{\text{Dust},2}/M_{*,2}) = -3.0 \pm 0.3$ for the two targets, respectively. These values are slightly lower than what is commonly observed for MS galaxies: for instance, Donevski et al. (2020) reports an observed value of $\log_{10}(M_{\text{Dust},1}/M_{*,1}) = -2.4 \pm 0.2$ for galaxies with analogous stellar masses and in the same redshift range (see analogous estimations in, e.g., Béthermin et al. 2015).

4. Characterisation of the groups

4.1. Estimation of the density field and group membership

The density field of the EDF-N is estimated following the same procedure described in Euclid Collaboration: Gentile et al. (2025) and briefly summarised here. For each galaxy, we rely on the Σ_N estimator defined as

$$\Sigma_N = \frac{N + 1}{\pi R_N^2}, \quad (2)$$

where R_N is the distance from the considered galaxy to the N -th closest neighbour. For consistency with Euclid Collaboration: Gentile et al. (2025), we employ the Σ_5 estimator applied to galaxies more massive than $10^{10.3}\ M_\odot$ and then interpolated to lower-mass galaxies. This choice allows us to focus on brighter objects with a more accurate photometric redshift estimation and

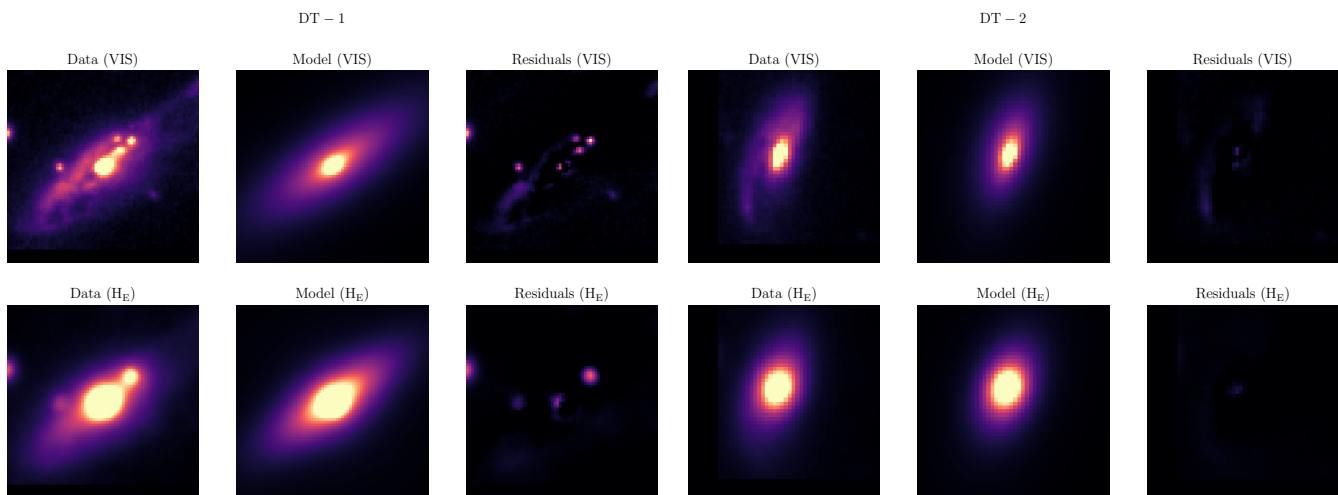


Fig. 4. Morphological analysis of the two disk galaxies. For each galaxy, we report the data (in the I_E and H_E bands), the modelling with a double Sérsic profile (see Sect. 3.2), and the residuals. Each stamp has a size of $5'' \times 5''$.

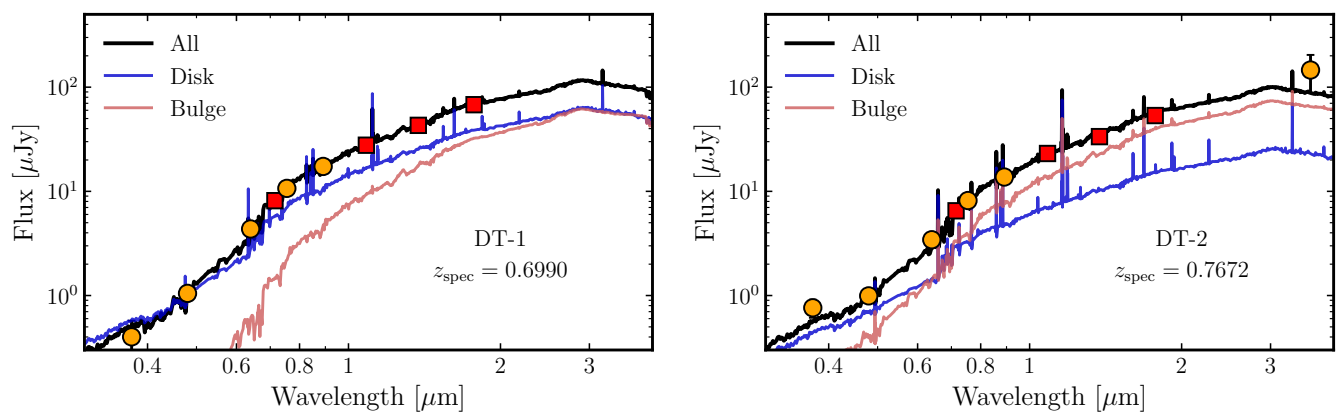


Fig. 5. SED fitting performed with CIGALE on the two disk galaxies. The photometry from *Euclid* is reported as red squares, while the additional photometry from ground-based observatories and IRAC is shown as orange points. The two coloured SEDs report the best-fitting SEDs for the bulge and disc components, whose photometry is derived as discussed in Sect. 3.2. For all SED fittings, the redshift is fixed to the spectroscopic value found in Sect. 3.1.

Table 2. Main properties estimated for the two groups analysed in this paper.

	Group 1	Group 2
$N_{\text{gal}} (M_* > M_{\text{lim}})$	10	10
$\log_{10}(M_*/M_{\odot})$ (Vis.)	12.01 ± 0.06	11.94 ± 0.04
$\log_{10}(M_*/M_{\odot})$ (Ext.)	12.05 ± 0.06	11.98 ± 0.04
$r_{3,\text{ang}} [']$	49.3	31.6
$r_{3,\text{phys}} [\text{kpc}]$	362	240
$\log_{10}(M_{\text{h}}/M_{\odot})$ (opt.)	13.8 ± 0.4	13.7 ± 0.4
$\log_{10}(M_{\text{h}}/M_{\odot})$ (X-rays)	...	13.8 ± 0.2

Notes. The second row reports the cumulative stellar mass of the objects detected in the DR1 images of the two groups, while the third row the total stellar mass obtained by statistically accounting for less massive galaxies. The radii of the two groups correspond to those where the local density is 3σ above the median value at their redshift. The two halo masses are computed, respectively, starting from the stellar mass of the group and from the X-ray luminosity (see Sect. 4.2).

well tracing the overall density field. Since our analysis mostly relies on photometric redshift (not allowing for a 3D modelling

of the density field), we rely on a tomographic approach. Given our interest in two specific over-densities, we employ thin redshift slices defined as

$$|z - z_{\text{DT}}| < 0.03 (1 + z_{\text{DT}}), \quad (3)$$

where z_{DT} is the spectroscopic redshift of the disk galaxy considered. The factor 0.03 accounts for the median accuracy of the photometric redshifts computed by the *Euclid* pipeline (Euclid Collaboration: Enia et al. 2025). We consider the density contrast parameter, defined as

$$\log_{10}(1 + \delta) = \log_{10} \left(1 + \frac{\Sigma_N - \bar{\Sigma}_N}{\bar{\Sigma}_N} \right), \quad (4)$$

where $\bar{\Sigma}_N$ is the median density field of a given redshift slice. This parameter follows a Gaussian distribution, as already shown, for instance, in Euclid Collaboration: Gentile et al. (2025). As expected from the selection scheme (Sect. 2.2), the two targets are found to belong to strong over-densities, with $\log_{10}(1 + \delta)$ of 1.4 and 1.0, corresponding to 6σ and 5σ above the median density at their redshifts. Quite remarkably, both galaxies are not found at the projected centre of the two over-densities (as indicated by the density curves shown in Fig. 1 for DT-1 and

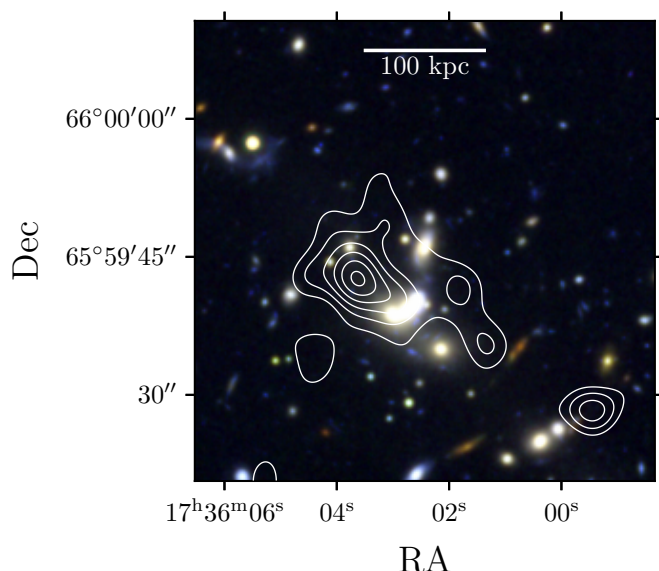


Fig. 6. Diffuse X-ray emission of the massive group hosting DT-2 as observed by XMM-Newton. The contours show the X-ray emission in the soft band (0.5–2 keV) in units of σ above the median, starting from 5σ and with steps of 2σ . The X-ray spectrum is consistent with thermal Bremsstrahlung with $T \sim 4 \times 10^6$ K and a total $L_X \sim 2 \times 10^{43}$ erg s $^{-1}$.

by the detected X-ray emission for DT-2; see Sect. 2.4), despite being the brightest sources in their groups.

4.2. Estimation of the halo mass

The halo masses of the two structures analysed in this paper are computed, under the hypothesis of virialised halos, following a slightly modified version of the procedure described in Daddi et al. (2021) and Sillassen et al. (2022). Firstly, we sum all the stellar masses of the galaxies possibly belonging to the two groups. To do this, we consider as candidate members all objects within r_3 (i.e., the region where the logarithmic local density field is above 3σ from its median value) with a redshift compatible with the z_{spec} of the respective DT, according to Eq. (3). Given the mass completeness estimated for our data (see Sect. 2.1), we correct the total stellar mass by integrating the stellar mass function at $z \sim 0.7$ by Shuntov et al. (2025) down to $10^7 M_\odot$ (corresponding to a small correcting factor of 0.91). The total stellar masses of the two groups are then converted into halo masses of $\sim 10^{13.8} M_\odot$, by using the conversion between stellar mass and halo mass by van der Burg et al. (2014) calibrated for clusters at $z \sim 1.7$. The derived halo masses – together with the other estimated properties of the two groups – are reported in Table 2. We underline that these halo masses are at least one order of magnitude higher than what we would have obtained by simply applying the standard stellar-to-halo mass relation of Behroozi et al. (2019) to the stellar masses of the two disky titans.

For the second group hosting DT-2, the availability of X-ray data (see Sect. 2.4) allows us to have better constraints on the halo mass. Firstly, because the detection of diffuse X-ray emission is likely due to the presence of hot gas, a good hint of the

expected virialisation of the group halo (see, e.g., Sarazin 1986 and references therein). Secondly, the integrated X-ray luminosity can be related to the halo mass following standard scaling relations (see, e.g., Lovisari et al. 2021 and references therein). For doing so, for each XMM EPIC camera, we extract the X-ray spectrum of the emission from our over-density in a circular aperture encompassing the emission visible in the stacked image (Fig. 6). The background spectra are extracted from fixed apertures of the same size located in an empty region of the nearby sky. We then perform the spectral modelling with XSPEC (Arnaud 1996). We employ an Astrophysical Plasma Emission Code (APEC; Smith et al. 2001) model describing a collisionally-ionised diffuse gas. The observed spectrum is compatible with an intra-cluster medium with a temperature of $T = (4 \pm 1) \times 10^6$ K emitting with thermal bremsstrahlung. The best-fitting spectrum returns a total integrated luminosity of $L_{0.1-2.4 \text{ keV}} = (2.2 \pm 0.3) \times 10^{43}$ erg s $^{-1}$ in the energy range 0.1–2.4 keV, once assuming that the group is located at the same spectroscopic redshift as the most massive galaxy. Through the scaling relation by Lovisari et al. (2021), linking the X-ray luminosity to the halo mass, we estimate the latter as $\log_{10}(M_h/M_\odot) = 13.8 \pm 0.2$, compatible – within the estimated uncertainties – with the values inferred from the optical data.

5. Discussion

The evidence presented in the previous sections of this paper pictures the two disky titans as massive ($M_* > 10^{11} M_\odot$) and star-forming galaxies (i.e., in the main sequence) located in strong over-densities (above 5σ from the median density field). These objects are quite rare: in over 20 deg^2 of the EDF-N, only four objects located in the redshift range $0.5 < z < 0.75$ show similar characteristics (see Euclid Collaboration: Gentile et al. 2025). In this section, we discuss possible scenarios to explain the properties of these objects.

A first point to address concerns the molecular gas mass observed in our targets. These values are compatible with what is commonly found in MS galaxies, as discussed in Sect. 3.1. This is quite uncommon for BGGs of massive groups, which are commonly found to be gas-poor (see, e.g., Castignani et al. 2020, 2022, 2023). In the standard cold accretion paradigm, indeed, the star-formation activity of MS galaxies is sustained over long timescales by the accretion of cold gas from the surrounding environment. The high halo masses of massive groups such as those hosting our targets make this explanation unfeasible. Several studies indeed already pointed out how the cold fraction of the baryonic accretion rate (BAR) – that is, the component available for star formation without requiring a long cooling time – tends to decrease with increasing halo mass as an effect of virial shock heating (e.g., Dekel & Birnboim 2006; Correa et al. 2018). To analyse quantitatively how this phenomenon impacts our galaxies, we compute the BAR through the parametrisation by Goerdt et al. (2010)

$$\text{BAR} \sim 137 \left(\frac{M_h}{10^{12} M_\odot} \right)^{1.15} \left(\frac{1+z}{4} \right)^{2.25} M_\odot \text{ yr}^{-1}. \quad (5)$$

Then, we use the parametrisation by Correa et al. (2018) to estimate the cold fraction

$$f_{\text{cold}} = 1 - \frac{1}{1 + [M_h/M_0(z)]^{a(z)}}, \quad (6)$$

with the redshift-dependent expressions for $a(z)$ and M_0 taken from Correa et al. (2018) in the $0 < z < 2$ case. The computation tells us that both galaxies, in this framework, should be

⁷ Even if the redshift range analysed in that study is a bit higher than that of our targets, we notice that their results are compatible with those obtained by Lin et al. (2012) analysing clusters at $z < 0.6$, ensuring that this relation does not significantly change at low z .

accreting a negligible amount of cold gas from the surrounding environment (less than $1 M_{\odot} \text{yr}^{-1}$), clearly insufficient to sustain a SFR of about $20 M_{\odot} \text{yr}^{-1}$ (see Table 1) over long timescales, even with unphysically high star-formation efficiencies.

Once excluded the cold accretion, an additional possibility for explaining the molecular gas in our targets could reside in the so-called cooling flows (see, e.g., the review by Fabian 1994 and references therein). These flows of cold gas from the outskirts of massive groups and clusters to the centre of their potential well are thought to be caused by the radiative cooling of the intra-cluster medium and the consequent low pressure originated at the centre of the cluster. Several studies suggested that these flows could reach the BCG and sustain its star formation (e.g., Donahue et al. 2015; McDonald et al. 2018). However, our galaxies are not located at the centre of their over-densities, as visible from the density curves in Fig. 1 and from the X-ray data shown in Fig. 6. Therefore, this explanation is quite unlikely for our sources. A third possibility for the origin of the molecular gas includes the accretion from other galaxies. This scenario will be discussed in more detail in Sect. 5.1.

A final point that should be addressed concerns the star-formation rates and efficiencies observed in our galaxies. According to the mechanism proposed by Martig et al. (2009), the presence of a massive bulge in our galaxies should help stabilise the stellar disk, preventing star-formation activity. Several studies and simulations showed how this morphological quenching should not be able to completely quench galaxies (e.g. Sain-tonge et al. 2012; Davis et al. 2014; Gobat et al. 2018; Eales et al. 2020), but its effect should still be visible as a reduction of the SFE (up to a factor 3–10; e.g., Gobat et al. 2018) with respect to the Schmidt–Kennicutt relation for star-forming galaxies (Fig. 3).

5.1. Two rejuvenating massive galaxies?

A possible model explaining all the observables collected on the two diskly titans involves the process of rejuvenation. This term is commonly defined as the phenomenon in which a quiescent galaxy restarts its star-formation activity by accreting cold gas from the surrounding environment or from another source. Several simulations (Robertson et al. 2006; Governato et al. 2009; Hopkins et al. 2009) and some observational studies (e.g., Belli et al. 2017; Mancini et al. 2019; Wang et al. 2025; Zhuang et al. 2025) showed that a wet merger can allow a galaxy to re-build a stellar disc and obtain levels of star formation high enough to bring it in the green valley or in the MS.

More in detail, our observations can be inscribed into a scenario where a “classic” massive ($M_{*} \sim 10^{11} M_{\odot}$), passive, and spheroidal BGG merges with a gas-rich satellite resulting in the accretion of cold gas onto the more massive galaxy. This process produces a temporary increase of the molecular gas fraction of the BGG and an increase of the SFE driven by the gas compression during the accretion phase (as shown in several simulation-based studies showing analogous enhancements in galaxy merging; e.g. Di Matteo et al. 2007; Moreno et al. 2021; Schechter et al. 2025). The following stabilisation of the disc driven by the presence of the massive bulge (Martig et al. 2009; Gobat et al. 2018) then produces a reduction in the observed SFE and the formation of a standard passive disc (commonly observed at low redshift; e.g. Masters et al. 2010). The eventual transition of these objects into classic spheroidal BGG can then be driven by external mechanisms such as dry mergers with other satellite galaxies. A recent study by Zhuang et al. (2025) presented a direct evidence of such a mechanism, by witnessing the accretion

of a small gas-rich satellite onto a more massive and quiescent galaxy with high-resolution observations from the James Webb Space Telescope (JWST).

In our case, such a scenario fits well with the evidence presented in the previous sections of this paper. More in detail:

1. Both galaxies present a passive bulge, with an SFR lower than expected for MS galaxies with the same mass (Sect. 3.3 and Fig. 3). The Sérsic index of this component is high ($n_{\text{bulge}} \sim 6$), compatible with a structure supported by velocity dispersion, as expected for massive spheroidal galaxies at low redshift (Kormendy & Kennicutt 2004; Fisher & Drory 2008). Moreover, the strength of the Balmer break (measured from the photometry, therefore quite uncertain) potentially indicates that the stellar population inside the bulge is significantly older than that in the disc (Sect. 3.3).
2. For both galaxies, the molecular gas mass is of the order of $10^{10-10.5} M_{\odot}$. Given the normal gas fraction expected from MS galaxies (e.g. Tacconi et al. 2020), these gas masses are compatible with those expected from less massive star-forming galaxies up to $10^{9.5-10} M_{\odot}$. At the same time, the low dust-to-stellar mass ratios compared to analogous MS galaxies indicates a possible *ex-situ* origin for a part of the stellar mass.
3. Both galaxies present a slightly distorted morphology. DT-1 presents a tidal feature in the external part of the disk, while DT-2 shows a small asymmetry in the spiral arms of the disc (Fig. 4). Both features can be interpreted as the result of a close encounter with another object.

The two targets would therefore represent two stages of the same evolutionary scenario: DT-1 would have been observed shortly after the close encounter with the satellite, easily explaining the more disturbed morphology and the higher SFE. DT-2 would represent, instead, a later stage where the SFE comes back to standard values and the morphology tends to stabilise. In addition, the morphological analysis of DT-1 shows a NIR-bright clump (see the residual panel in Fig. 4) that could be interpreted as a residual of the bulge of the accreted galaxy, supporting the merger-induced rejuvenation scenario: this possibility clearly needs to be confirmed with follow-up spectroscopic observations. In alternative, another galaxy with a redshift compatible with the group and located at a proper projected distance of about 200 kpc south of DT-1 also shows a significant tidal feature. The distance of the galaxy would allow for a close encounter with DT-1, given the velocity dispersion expected from a massive group of $M_{\text{h}} \sim 10^{13.8} M_{\odot}$ by applying the virial theorem (about 750 km s^{-1}) and the age of the disc in DT-1 (Sect. 3.3).

Such a scenario also fits well with the current consensus on the evolutionary path that brings to the formation of the most massive BGG, with most of the stellar mass assembled at high redshift ($z \sim 3 - 5$; e.g., De Lucia & Blaizot 2007) and a smaller fraction assembled at later time (after $z \sim 1$; e.g. Collins et al. 2009; Stott et al. 2011) through accretion of satellite galaxies. Finally, the proposed scenario easily explains the observed rarity of this kind of sources by relying on a non-secular process such as a galaxy merger.

5.2. Comparison with simulation

To verify the plausibility of our scenario, we look for analogues of our diskly titans in the IllustrisTNG simulation suite (Nelson et al. 2019). Given the requirement of our galaxies to be located in over-densities, we analyse the TNG300 simulation, including

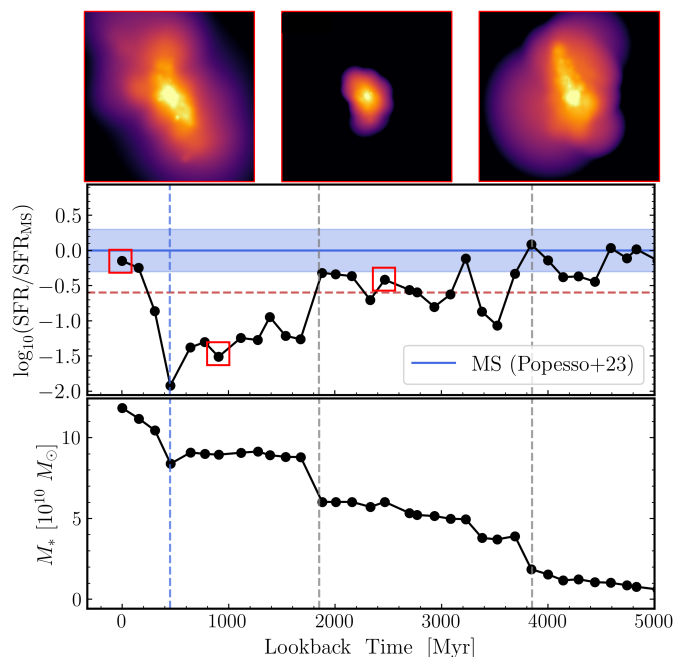


Fig. 7. Example of an analogue of the diskly titans in the TNG300 simulation. *Lower panel:* Growth of the stellar mass in the last 5 Myr. The dashed vertical lines indicate the past mergers, the last episode causing the rejuvenation is highlighted in blue. *Mid panel:* Star formation history, parametrised as distance from the main sequence by Popesso et al. (2023), where the main sequence (and its intrinsic scatter) are reported in blue and the red sequence (below 2σ from the relation) is reported as a dashed red line. *Upper panel:* Density maps of the stellar component in the TNG analogue at key cosmic epochs, the corresponding instants in the star formation history are highlighted by red boxes. The cutouts have a constant size of 500 kpc.

a cosmological volume of about 300 Mpc^3 at a (baryonic) resolution of $m_b = 1.1 \times 10^7 M_\odot h^{-1}$, ideal to sample a large variety of environments. The selection criteria mimic those employed in Sect. 2.2: we select galaxies from the snapshot at $z = 0.76$ with $M_* > 10^{11} M_\odot$, within 0.3 dex from the main sequence, and located in over-densities. For the second criterion, we employ the parametrization of the main sequence by Euclid Collaboration: Enia et al. (2025) and the SFRs averaged over 100 Myr computed by Donnari et al. 2019 and Pillepich et al. 2019 to better match the observational constraints. The last criterion is accounted for through a cut in the mass of the hosting dark matter ($M_h > 10^{13} M_\odot$), approximately corresponding to the expected halo mass of a 5σ over-density at $z \sim 0.75$ (Euclid Collaboration: Gentile et al. 2025). These criteria return a total sample of 238 galaxies, with a median halo mass of $M_h \sim 10^{13.5} M_\odot$, and representing about 10% of the galaxies with similar halos, in good agreement with the findings presented in the previous sections. For these analogues, we analyse the evolution with time of the stellar mass, SFR, halo mass, and gas mass in the last 5 Gyr before the observations (roughly corresponding to $z \sim 3$). We find that in nearly half of the cases, these sources spent a significant amount of time (about 2–3 Gyr) in the red sequence before experiencing an episode of rejuvenation and coming back to the main sequence. In one quarter of the cases, the decrease of the specific star formation rate was not sufficient to bring the galaxies to the red sequence, but only to the green valley (i.e., between one and two σ below the main sequence). In the remaining cases, no significant deviation from the secular evolution in the main sequence is visible in the TNG data.

The first case clearly agrees with the scenario outlined in the previous sections. We report an example of galaxy belonging to this class in Fig. 7. It is possible to notice how this source, after a first period of secular evolution as part of the main sequence (up to a lookback time of 4 Myr ; $z \sim 2$), has a first merger episode and moves to the red sequence. In the next 2 Gyr, the accretion of small satellites drives its increase in stellar mass and the oscillation between the red sequence and the green valley, up to a lookback time of 2 Gyr ($z \sim 1.3$). In this phase, the sequence of small merging episodes produces a disturbed morphology (right-most cutout). Then a second merger episode causes again the transition to the red sequence, for a long period of quiescence lasting about 2 Gyr in which the morphology relaxes and the size becomes more compact (central cutout). In this phase, the galaxy appears as the normal BGGs at these redshifts. Finally, about 500 Myr before the observation, a last merging episode causes the rejuvenation of the galaxy and its coming back to the main sequence. The accretion of the gas from the satellite and the new star formation activity take place in the outskirts of the galaxy, producing a more extended morphology (left-most cutout), analogous to what is observed in our two sources.

6. Summary

In this paper, we present the discovery of two diskly titans in the first data from the *Euclid* satellite. These galaxies are defined as massive ($M_* > 10^{11} M_\odot$) and star-forming ($\text{SFR} \sim 20 M_\odot \text{ yr}^{-1}$) systems located in strong over-densities (above 5σ from the median density) at $z \sim 0.75$ and showing a visible stellar disc. These sources are quite rare, with only four candidates observed in more than 20 deg^2 covered by *Euclid* in the EDF-N.

Our observational results can be summarised as follows:

- Both galaxies are the brightest sources in two massive group-size structures with $M_h \sim 10^{13.8} M_\odot$. According to the predictions for virial-shock heating, both sources are expected to accrete only a negligible amount of cold gas from the surrounding environment, insufficient to sustain significant star formation over long time-scales.
- Despite this, the two galaxies host significant gas reservoirs ($M_{\text{H}_2} \sim 10^{10.3} M_\odot$). Moreover, both sources show a star-formation efficiency and a depletion time compatible with what is commonly expected for MS galaxies according to the Schmidt–Kennicutt relation, or a slightly higher SFE in the case of DT-1.
- Both galaxies present a massive and passive bulge at their centre, with stellar ages higher than those observed in the disc. In both galaxies, the bulk of the stellar mass is located in the bulge, while star-formation activity is confined within the stellar disc.

We interpret these observations as evidence that our diskly titans are the product of an episode of merging-induced rejuvenation, in which the most massive galaxy of the groups accretes cold gas from a surrounding member of the structure and restarts its star-formation activity. This scenario easily explains the observed properties of the two sources and justifies the observed MS-like SFE as a composite effect of a merger-induced starburst and morphological quenching. Such a scenario is supported by the identification in the TNG300 simulation of analogous systems with evidence of past merger activity linked to rejuvenation. However, the proposed scenario needs further observations to be completely confirmed. Spatially-resolved optical spectroscopy (e.g. through the Integral Field Unit equipped

on the JWST or with VLT-MUSE) would allow us to measure the stellar ages of the bulge and disc of our galaxies, confirming the initial picture inferred from broad-band photometry alone. Similarly, deeper millimetre observations would allow us to better constrain the continuum emission of our sources, giving us a better handle on the obscured star-formation activity. At the same time, higher-resolution observations of the (sub)mm continuum and of the CO(2-1) line would allow us to understand if the gas and the star-formation are actually located in the outer disc or if some component is located in the central bulge. Such data would also allow us to perform a dynamical modelling of the gas component, giving us an additional probe of the dynamical mass independent of the SED-fitting derived stellar mass. Both the observations listed so far (resolved spectroscopy and deeper NOEMA observations) could also allow us to detect the molecular gas on its way to be accreted on out main targets, either by observing a low- J CO transition or by detecting the Ly α line (e.g., Daddi et al. 2022; Guo et al. 2025). Finally, the identification of the other members of the group still relies only on photometric redshift; a more intensive spectroscopic coverage of the environment surrounding our galaxies would allow us to reduce the uncertainty on the estimation of the halo mass and confirm the inferred lack of cold accretion from the surrounding environment.

In summary, our study showcases the ability of *Euclid* to find rare sources thanks to the unprecedented statistics offered by its surveys. Moreover, the synergy between *Euclid* and other facilities observing the Universe at other wavelengths gives us the ability to test our galaxy evolution models in new and unexplored regions of the parameter space.

Acknowledgements. This work is based on observations carried out under project number S25BT with the IRAM NOEMA Interferometer. IRAM is supported by INSU/CNRS (France), MPG (Germany) and IGN (Spain). FaGe, EmDa, AnEn, GaDL, ChD'E, LuPo acknowledge support from the ELSA project. "ELSA: Euclid Legacy Science Advanced analysis tools" (Grant Agreement no. 101135203) is funded by the European Union. Views and opinions expressed are however those of the author(s) only and do not necessarily reflect those of the European Union or Innovate UK. Neither the European Union nor the granting authority can be held responsible for them. UK participation is funded through the UK HORIZON guarantee scheme under Innovate UK grant 10093177. VaSa acknowledges support from France 2030 through the project named Académie Spatiale d'Île-de-France (<https://academiespatiale.fr/>) managed by the National Research Agency under bearing the reference ANR-23-CMAS-0041 The Euclid Consortium acknowledges the European Space Agency and a number of agencies and institutes that have supported the development of *Euclid*, in particular the Agenzia Spaziale Italiana, the Austrian Forschungsförderungsgesellschaft funded through BMIMI, the Belgian Science Policy, the Canadian Euclid Consortium, the Deutsches Zentrum für Luft- und Raumfahrt, the DTU Space and the Niels Bohr Institute in Denmark, the French Centre National d'Études Spatiales, the Fundação para a Ciência e a Tecnologia, the Hungarian Academy of Sciences, the Ministerio de Ciencia, Innovación y Universidades, the National Aeronautics and Space Administration, the National Astronomical Observatory of Japan, the Nederlandse Onderzoekschool Voor Astronomie, the Norwegian Space Agency, the Research Council of Finland, the Romanian Space Agency, the Swiss Space Office (SSO) at the State Secretariat for Education, Research, and Innovation (SERI) and the United Kingdom Space Agency. A complete and detailed list is available on the *Euclid* web site (www.euclid-ec.org/consortium/community/). Based on data from UNIONS, a scientific collaboration using three Hawaii-based telescopes: CFHT, Pan-STARRS, and Subaru www.skysurvey.cc. Based on data from the Dark Energy Camera (DECam) on the Blanco 4-m Telescope at CTIO in Chile <https://www.darkenergysurvey.org>. The IllustrisTNG simulations were undertaken with compute time awarded by the Gauss Centre for Supercomputing (GCS) under GCS Large-Scale Projects GCS-ILLU and GCS-DWAR on the GCS share of the supercomputer Hazel Hen at the High Performance Computing Center Stuttgart (HLRS), as well as on the machines of the Max Planck Computing and Data Facility (MPCDF) in Garching, Germany.

References

- Arnaud, K. A. 1996, in ASP Conf. Ser., Vol. 101, 17
- Bahé, Y. M., Barnes, D. J., Dalla Vecchia, C., et al. 2017, MNRAS, 470, 4186
- Behroozi, P., Wechsler, R. H., Hearin, A. P., & Conroy, C. 2019, MNRAS, 488, 3143
- Belli, S., Genzel, R., Förster Schreiber, N. M., et al. 2017, ApJ, 841, L6
- Béthermin, M., Daddi, E., Magdis, G., et al. 2015, A&A, 573, A113
- Bisigello, L., Giuliotti, M., Prandoni, I., et al. 2025, The Open Journal of Astrophysics, 8, 101
- Bolatto, A. D., Wolfire, M., & Leroy, A. K. 2013, ARA&A, 51, 207
- Bolzonella, M., Kovač, K., Pozzetti, L., et al. 2010, A&A, 524, A76
- Bondi, M., Scaramella, R., Zamorani, G., et al. 2024, A&A, 683, A179
- Boquien, M., Burgarella, D., Roehlly, Y., et al. 2019, A&A, 622, A103
- Boselli, A., Fossati, M., & Sun, M. 2022, A&A Rev., 30, 3
- Bower, R. G., Benson, A. J., Malbon, R., et al. 2006, MNRAS, 370, 645
- Brinchmann, J., Charlot, S., White, S. D. M., et al. 2004, MNRAS, 351, 1151
- Bruzual, G. & Charlot, S. 2003, MNRAS, 344, 1000
- CASA Team, Bean, B., Bhatnagar, S., et al. 2022, PASP, 134, 114501
- Castignani, G., Pandey-Pommier, M., Hamer, S. L., et al. 2020, A&A, 640, A65
- Castignani, G., Radovich, M., Combes, F., et al. 2022, A&A, 667, A52
- Castignani, G., Radovich, M., Combes, F., et al. 2023, A&A, 672, A139
- Chabrier, G. 2003, PASP, 115, 763
- Charlot, S. & Fall, S. M. 2000, ApJ, 539, 718
- Collins, C. A., Stott, J. P., Hilton, M., et al. 2009, Nature, 458, 603
- Correa, C. A., Schaye, J., Wyithe, J. S. B., et al. 2018, MNRAS, 473, 538
- Croton, D. J., Springel, V., White, S. D. M., et al. 2006, MNRAS, 365, 11
- Daddi, E., Bournaud, F., Walter, F., et al. 2010a, ApJ, 713, 686
- Daddi, E., Dannerbauer, H., Liu, D., et al. 2015, A&A, 577, A46
- Daddi, E., Elbaz, D., Walter, F., et al. 2010b, ApJ, 714, L118
- Daddi, E., Rich, R. M., Valentino, F., et al. 2022, ApJ, 926, L21
- Daddi, E., Valentino, F., Rich, R. M., et al. 2021, A&A, 649, A78
- Davis, T. A., Young, L. M., Crocker, A. F., et al. 2014, MNRAS, 444, 3427
- De Lucia, G. & Blaizot, J. 2007, MNRAS, 375, 2
- Dekel, A. & Birnboim, Y. 2006, MNRAS, 368, 2
- den Brok, J. S., Chatzigiannakis, D., Bigiel, F., et al. 2021, MNRAS, 504, 3221
- Di Matteo, P., Combes, F., Melchior, A.-L., & Semelin, B. 2007, A&A, 468, 61
- Donahue, M., Connor, T., Fogarty, K., et al. 2015, ApJ, 805, 177
- Donevski, D., Lapi, A., Małek, K., et al. 2020, A&A, 644, A144
- Donnari, M., Pillepich, A., Nelson, D., et al. 2019, MNRAS, 485, 4817
- Dressler, A. 1980, ApJ, 236, 351
- Eales, S., Eales, O., & de Vis, P. 2020, MNRAS, 491, 69
- Euclid Collaboration: Aussel, H., Tereno, I., Schirmer, M., et al. 2025, A&A, in press (Euclid Q1 SI), <https://doi.org/10.1051/0004-6361/202554610>, arXiv:2503.15302
- Euclid Collaboration: Bisigello, L., Rodighiero, G., Fotopoulou, S., et al. 2025, A&A, in press (Euclid Q1 SI), <https://doi.org/10.1051/0004-6361/202554537>, arXiv:2503.15323
- Euclid Collaboration: Cleland, C., Mei, S., De Lucia, G., et al. 2025, A&A, in press, <https://doi.org/10.1051/0004-6361/202554581>, arXiv:2503.15313
- Euclid Collaboration: Cropper, M., Al-Bahlawan, A., Amiaux, J., et al. 2025, A&A, 697, A2
- Euclid Collaboration: Desprez, G., Paltani, S., Coupon, J., et al. 2020, A&A, 644, A31
- Euclid Collaboration: Enia, A., Bolzonella, M., Pozzetti, L., et al. 2024, A&A, 691, A175
- Euclid Collaboration: Enia, A., Pozzetti, L., Bolzonella, M., et al. 2025, A&A, in press (Euclid Q1 SI), <https://doi.org/10.1051/0004-6361/202554576>, arXiv:2503.15314
- Euclid Collaboration: Gentile, F., Daddi, E., Elbaz, D., et al. 2025, A&A, in press (Euclid Q1 SI), <https://doi.org/10.1051/0004-6361/202557633>, arXiv:2511.02964
- Euclid Collaboration: Jahnke, K., Gillard, W., Schirmer, M., et al. 2025, A&A, 697, A3
- Euclid Collaboration: McPartland, C. J. R., Zalesky, L., Weaver, J. R., et al. 2025, A&A, 695, A259
- Euclid Collaboration: Mellier, Y., Abdurro'uf, Acevedo Barroso, J., et al. 2025, A&A, 697, A1
- Euclid Collaboration: Moneti, A., McCracken, H. J., Shuntov, M., et al. 2022, A&A, 658, A126
- Euclid Collaboration: Quilley, L., Damjanov, I., de Lapparent, V., et al. 2025, A&A, in press (Euclid Q1 SI), <https://doi.org/10.1051/0004-6361/202554585>, arXiv:2503.15309
- Euclid Collaboration: Romelli, E., Kümmel, M., Dole, H., et al. 2025, A&A, in press (Euclid Q1 SI), <https://doi.org/10.1051/0004-6361/202554586>, arXiv:2503.15305
- Euclid Collaboration: Scaramella, R., Amiaux, J., Mellier, Y., et al. 2022, A&A, 662, A112
- Euclid Quick Release Q1. 2025, <https://doi.org/10.57780/esa-2853f3b>

- Fabian, A. C. 1994, *ARA&A*, 32, 277
- Feldmann, R., Carollo, C. M., Mayer, L., et al. 2010, *ApJ*, 709, 218
- Ferland, G. J., Korista, K. T., Verner, D. A., et al. 1998, *PASP*, 110, 761
- Fisher, D. B. & Drory, N. 2008, *AJ*, 136, 773
- Fogarty, K., Postman, M., Connor, T., Donahue, M., & Moustakas, J. 2015, *ApJ*, 813, 117
- Fogarty, K., Postman, M., Li, Y., et al. 2019, *ApJ*, 879, 103
- Foreman-Mackey, D., Hogg, D. W., Lang, D., & Goodman, J. 2013, *PASP*, 125, 306
- Fraser-McKelvie, A., Brown, M. J. I., & Pimblett, K. A. 2014, *MNRAS*, 444, L63
- Gentile, F., Talia, M., Daddi, E., et al. 2024, *A&A*, 687, A288
- Ghaffari, Z., Gozaliasl, G., Biviano, A., et al. 2026, *A&A*, 708, A129
- Gildas Team. 2013, *GILDAS: Grenoble Image and Line Data Analysis Software, Astrophysics Source Code Library*, record ascl:1305.010
- Gobat, R., Daddi, E., Magdis, G., et al. 2018, *Nature Astronomy*, 2, 239
- Goerdt, T., Dekel, A., Sternberg, A., et al. 2010, *MNRAS*, 407, 613
- Governato, F., Brook, C. B., Brooks, A. M., et al. 2009, *MNRAS*, 398, 312
- Gunn, J. E. & Gott, III, J. R. 1972, *ApJ*, 176, 1
- Guo, S., Daddi, E., Gobat, R., et al. 2025, arXiv:2510.01421
- Gwyn, S., McConnachie, A. W., Cuillandre, J.-C., et al. 2025, *AJ*, 170, 324
- Henriques, B. M. B., White, S. D. M., Thomas, P. A., et al. 2017, *MNRAS*, 469, 2626
- Hopkins, P. F., Cox, T. J., Younger, J. D., & Hernquist, L. 2009, *ApJ*, 691, 1168
- Ilbert, O., Salvato, M., Le Floch, E., et al. 2010, *ApJ*, 709, 644
- Inoue, A. K. 2011, *MNRAS*, 415, 2920
- Jin, S., Daddi, E., Magdis, G. E., et al. 2019, *ApJ*, 887, 144
- Kauffmann, G., Heckman, T. M., White, S. D. M., et al. 2003, *MNRAS*, 341, 54
- Kennicutt, R. C. & Evans, N. J. 2012, *ARA&A*, 50, 531
- Kennicutt, Jr., R. C. 1998, *ApJ*, 498, 541
- Kormendy, J. & Kennicutt, Jr., R. C. 2004, *ARA&A*, 42, 603
- Lin, Y.-T., Stanford, S. A., Eisenhardt, P. R. M., et al. 2012, *ApJ*, 745, L3
- López-Cruz, O., Barkhouse, W. A., & Yee, H. K. C. 2004, *ApJ*, 614, 679
- Lovisari, L., Ettori, S., Gaspari, M., & Giles, P. A. 2021, *Universe*, 7, 139
- Lupton, R., Gunn, J. E., Ivezić, Z., Knapp, G. R., & Kent, S. 2001, in *ASP Conf. Ser.*, Vol. 238, *Astronomical Data Analysis Software and Systems X*, 269
- Mancini, C., Daddi, E., Juneau, S., et al. 2019, *MNRAS*, 489, 1265
- Martig, M., Bournaud, F., Teyssier, R., & Dekel, A. 2009, *ApJ*, 707, 250
- Martig, M., Crocker, A. F., Bournaud, F., et al. 2013, *MNRAS*, 432, 1914
- Masters, K. L., Mosleh, M., Romer, A. K., et al. 2010, *MNRAS*, 405, 783
- McDonald, M., Gaspari, M., McNamara, B. R., & Tremblay, G. R. 2018, *ApJ*, 858, 45
- McIntosh, D. H., Wagner, C., Cooper, A., et al. 2014, *MNRAS*, 442, 533
- Mehrtens, N., Romer, A. K., Hilton, M., et al. 2012, *MNRAS*, 423, 1024
- Moreno, J., Torrey, P., Ellison, S. L., et al. 2021, *MNRAS*, 503, 3113
- Nelson, D., Springel, V., Pillepich, A., et al. 2019, *Computational Astrophysics and Cosmology*, 6, 2
- Oke, J. B. & Gunn, J. E. 1983, *ApJ*, 266, 713
- Peng, Y.-j., Lilly, S. J., Kovač, K., et al. 2010, *ApJ*, 721, 193
- Pillepich, A., Nelson, D., Springel, V., et al. 2019, *MNRAS*, 490, 3196
- Planck Collaboration: Aghanim, N., Akrami, Y., Ashdown, M., et al. 2020, *A&A*, 641, A6
- Popesso, P., Concas, A., Cresci, G., et al. 2023, *MNRAS*, 519, 1526
- Pozzetti, L., Bolzonella, M., Zucca, E., et al. 2010, *A&A*, 523, A13
- Robertson, B., Bullock, J. S., Cox, T. J., et al. 2006, *ApJ*, 645, 986
- Saintonge, A., Tacconi, L. J., Fabello, S., et al. 2012, *ApJ*, 758, 73
- Sarazin, C. L. 1986, *Reviews of Modern Physics*, 58, 1
- Schechter, A. L., Genel, S., Terrazas, B., et al. 2025, *ApJ*, 989, 149
- Schmidt, M. 1959, *ApJ*, 129, 243
- Schreiber, C., Elbaz, D., Pannella, M., et al. 2018, *A&A*, 609, A30
- Shuntov, M., Ilbert, O., Toft, S., et al. 2025, *A&A*, 695, A20
- Sillassen, N. B., Jin, S., Magdis, G. E., et al. 2022, *A&A*, 665, L7
- Smith, R. K., Brickhouse, N. S., Liedahl, D. A., & Raymond, J. C. 2001, *ApJ*, 556, L91
- Stott, J. P., Collins, C. A., Burke, C., Hamilton-Morris, V., & Smith, G. P. 2011, *MNRAS*, 414, 445
- Tacconi, L. J., Genzel, R., & Sternberg, A. 2020, *ARA&A*, 58, 157
- van den Bosch, F. C., Aquino, D., Yang, X., et al. 2008, *MNRAS*, 387, 79
- van der Burg, R. F. J., Muzzin, A., Hoekstra, H., et al. 2014, *A&A*, 561, A79
- Wang, Y., Wang, T., Xu, K., et al. 2025, *ApJ*, 980, 107
- Weller, E. J., Pacucci, F., Ni, Y., Hernquist, L., & Park, M. 2025, *ApJ*, 979, 181
- Whiley, I. M., Aragón-Salamanca, A., De Lucia, G., et al. 2008, *MNRAS*, 387, 1253
- Wolter, A., Gioia, I. M., Henry, J. P., & Mullis, C. R. 2005, *A&A*, 444, 165
- Wuyts, S., Förster Schreiber, N. M., van der Wel, A., et al. 2011, *ApJ*, 742, 96
- Zhuang, M.-Y., Shangqian, J., Bian, Y., et al. 2025, arXiv:2512.13932
- 1 CEA Saclay, DFR/IRFU, Service d'Astrophysique, Bat. 709, 91191 Gif-sur-Yvette, France
- 2 INAF-Osservatorio di Astrofisica e Scienza dello Spazio di Bologna, Via Piero Gobetti 93/3, 40129 Bologna, Italy
- 3 Université Paris-Saclay, Université Paris Cité, CEA, CNRS, AIM, 91191, Gif-sur-Yvette, France
- 4 Université de Strasbourg, CNRS, Observatoire astronomique de Strasbourg, UMR 7550, 67000 Strasbourg, France
- 5 Center for Astronomy and Astrophysics and Department of Physics, Fudan University, Shanghai 200438, People's Republic of China
- 6 School of Physics & Astronomy, University of Southampton, Highfield Campus, Southampton SO17 1BJ, UK
- 7 School of Physics and Astronomy, Anqing Normal University, Anqing 246133, China
- 8 Institute of Astronomy and Astrophysics, Anqing Normal University, Anqing 246133, China
- 9 Key Laboratory of Modern Astronomy and Astrophysics (Nanjing University), Ministry of Education, Nanjing 210093, China
- 10 Leiden Observatory, Leiden University, Einsteinweg 55, 2333 CC Leiden, The Netherlands
- 11 Sterrenkundig Observatorium, Universiteit Gent, Krijgslaan 281 S9, 9000 Gent, Belgium
- 12 INAF-Osservatorio Astronomico di Padova, Via dell'Osservatorio 5, 35122 Padova, Italy
- 13 Instituto de Astrofísica de Canarias, E-38205 La Laguna, Tenerife, Spain
- 14 Universidad de La Laguna, Dpto. Astrofísica, E-38206 La Laguna, Tenerife, Spain
- 15 INAF-Osservatorio Astronomico di Trieste, Via G. B. Tiepolo 11, 34143 Trieste, Italy
- 16 Institute de Physique du Globe de Paris, 1 Rue Jussieu, 75005, Paris, France
- 17 SISSA, International School for Advanced Studies, Via Bonomea 265, 34136 Trieste TS, Italy
- 18 National Centre for Nuclear Research, ul. Pasteura 7, 02-093, Warsaw, Poland
- 19 Dipartimento di Fisica "G. Occhialini", Università degli Studi di Milano Bicocca, Piazza della Scienza 3, 20126 Milano, Italy
- 20 INAF-Osservatorio Astronomico di Brera, Via Brera 28, 20122 Milano, Italy
- 21 Instituto de Física, Pontificia Universidad Católica de Valparaíso, Valparaíso, Chile
- 22 INAF-Istituto di Astrofisica e Planetologia Spaziali, via del Fosso del Cavaliere, 100, 00100 Roma, Italy
- 23 Dipartimento di Fisica e Astronomia "Augusto Righi" - Alma Mater Studiorum Università di Bologna, via Piero Gobetti 93/2, 40129 Bologna, Italy
- 24 Univ. Lille, CNRS, Centrale Lille, UMR 9189 CRISTAL, 59000 Lille, France
- 25 Université Paris-Saclay, CNRS, Institut d'astrophysique spatiale, 91405, Orsay, France
- 26 IFPU, Institute for Fundamental Physics of the Universe, via Beirut 2, 34151 Trieste, Italy
- 27 Zentrum für Astronomie, Universität Heidelberg, Philosophenweg 12, 69120 Heidelberg, Germany
- 28 ESAC/ESA, Camino Bajo del Castillo, s/n., Urb. Villafranca del Castillo, 28692 Villanueva de la Cañada, Madrid, Spain
- 29 INFN, Sezione di Trieste, Via Valerio 2, 34127 Trieste TS, Italy
- 30 Dipartimento di Fisica e Astronomia, Università di Bologna, Via Gobetti 93/2, 40129 Bologna, Italy
- 31 INFN-Sezione di Bologna, Viale Berti Pichat 6/2, 40127 Bologna, Italy
- 32 Dipartimento di Fisica, Università di Genova, Via Dodecaneso 33, 16146, Genova, Italy
- 33 INFN-Sezione di Genova, Via Dodecaneso 33, 16146, Genova, Italy
- 34 Department of Physics "E. Pancini", University Federico II, Via Cinthia 6, 80126, Napoli, Italy

- ³⁵ INAF-Osservatorio Astronomico di Capodimonte, Via Moiariello 16, 80131 Napoli, Italy
- ³⁶ Dipartimento di Fisica, Università degli Studi di Torino, Via P. Giuria 1, 10125 Torino, Italy
- ³⁷ INFN-Sezione di Torino, Via P. Giuria 1, 10125 Torino, Italy
- ³⁸ INAF-Osservatorio Astrofisico di Torino, Via Osservatorio 20, 10025 Pino Torinese (TO), Italy
- ³⁹ INAF-IASF Milano, Via Alfonso Corti 12, 20133 Milano, Italy
- ⁴⁰ Centro de Investigaciones Energéticas, Medioambientales y Tecnológicas (CIEMAT), Avenida Complutense 40, 28040 Madrid, Spain
- ⁴¹ Port d'Informació Científica, Campus UAB, C. Albareda s/n, 08193 Bellaterra (Barcelona), Spain
- ⁴² INAF-Osservatorio Astronomico di Roma, Via Frascati 33, 00078 Monteporzio Catone, Italy
- ⁴³ INFN section of Naples, Via Cinthia 6, 80126, Napoli, Italy
- ⁴⁴ Dipartimento di Fisica e Astronomia "Augusto Righi" - Alma Mater Studiorum Università di Bologna, Viale Berti Pichat 6/2, 40127 Bologna, Italy
- ⁴⁵ Institute for Astronomy, University of Edinburgh, Royal Observatory, Blackford Hill, Edinburgh EH9 3HJ, UK
- ⁴⁶ European Space Agency/ESRIN, Largo Galileo Galilei 1, 00044 Frascati, Roma, Italy
- ⁴⁷ Université Claude Bernard Lyon 1, CNRS/IN2P3, IP2I Lyon, UMR 5822, Villeurbanne, F-69100, France
- ⁴⁸ Institut de Ciències del Cosmos (ICCUB), Universitat de Barcelona (IEEC-UB), Martí i Franquès 1, 08028 Barcelona, Spain
- ⁴⁹ Institució Catalana de Recerca i Estudis Avançats (ICREA), Pas-seig de Luíís Companys 23, 08010 Barcelona, Spain
- ⁵⁰ Institut de Ciències de l'Espai (IEEC-CSIC), Campus UAB, Carrer de Can Magrans, s/n Cerdanyola del Vallés, 08193 Barcelona, Spain
- ⁵¹ UCB Lyon 1, CNRS/IN2P3, IUF, IP2I Lyon, 4 rue Enrico Fermi, 69622 Villeurbanne, France
- ⁵² Mullard Space Science Laboratory, University College London, Holmbury St Mary, Dorking, Surrey RH5 6NT, UK
- ⁵³ Department of Astronomy, University of Geneva, ch. d'Ecogia 16, 1290 Versoix, Switzerland
- ⁵⁴ Space Science Data Center, Italian Space Agency, via del Politecnico snc, 00133 Roma, Italy
- ⁵⁵ School of Physics, HH Wills Physics Laboratory, University of Bristol, Tyndall Avenue, Bristol, BS8 1TL, UK
- ⁵⁶ University Observatory, LMU Faculty of Physics, Scheinerstr. 1, 81679 Munich, Germany
- ⁵⁷ Max Planck Institute for Extraterrestrial Physics, Giessenbachstr. 1, 85748 Garching, Germany
- ⁵⁸ Universitäts-Sternwarte München, Fakultät für Physik, Ludwig-Maximilians-Universität München, Scheinerstr. 1, 81679 München, Germany
- ⁵⁹ National Research Council, Herzberg Astronomy and Astrophysics Research Centre, 5071 W. Saanich Rd. Victoria, BC, V9E 2E7, Canada
- ⁶⁰ Institute of Theoretical Astrophysics, University of Oslo, P.O. Box 1029 Blindern, 0315 Oslo, Norway
- ⁶¹ Jet Propulsion Laboratory, California Institute of Technology, 4800 Oak Grove Drive, Pasadena, CA, 91109, USA
- ⁶² Department of Physics, Lancaster University, Lancaster, LA1 4YB, UK
- ⁶³ Felix Hormuth Engineering, Goethestr. 17, 69181 Leimen, Germany
- ⁶⁴ Technical University of Denmark, Elektrovej 327, 2800 Kgs. Lyngby, Denmark
- ⁶⁵ Cosmic Dawn Center (DAWN), Denmark
- ⁶⁶ Max-Planck-Institut für Astronomie, Königstuhl 17, 69117 Heidelberg, Germany
- ⁶⁷ NASA Goddard Space Flight Center, Greenbelt, MD 20771, USA
- ⁶⁸ Department of Physics and Astronomy, University College London, Gower Street, London WC1E 6BT, UK
- ⁶⁹ Aix-Marseille Université, CNRS/IN2P3, CPPM, Marseille, France
- ⁷⁰ Université de Genève, Département de Physique Théorique and Centre for Astroparticle Physics, 24 quai Ernest-Ansermet, CH-1211 Genève 4, Switzerland
- ⁷¹ Department of Physics, P.O. Box 64, University of Helsinki, 00014 Helsinki, Finland
- ⁷² Helsinki Institute of Physics, Gustaf Hällströmin katu 2, University of Helsinki, 00014 Helsinki, Finland
- ⁷³ Laboratoire d'étude de l'Univers et des phénomènes eXtremes, Observatoire de Paris, Université PSL, Sorbonne Université, CNRS, 92190 Meudon, France
- ⁷⁴ SKAO, Jodrell Bank, Lower Withington, Macclesfield SK11 9FT, UK
- ⁷⁵ Centre de Calcul de l'IN2P3/CNRS, 21 avenue Pierre de Coubertin 69627 Villeurbanne Cedex, France
- ⁷⁶ Universität Bonn, Argelander-Institut für Astronomie, Auf dem Hügel 71, 53121 Bonn, Germany
- ⁷⁷ INFN-Sezione di Roma, Piazzale Aldo Moro, 2 - c/o Dipartimento di Fisica, Edificio G. Marconi, 00185 Roma, Italy
- ⁷⁸ Aix-Marseille Université, CNRS, CNES, LAM, Marseille, France
- ⁷⁹ Department of Physics, Institute for Computational Cosmology, Durham University, South Road, Durham, DH1 3LE, UK
- ⁸⁰ Université Paris Cité, CNRS, Astroparticule et Cosmologie, 75013 Paris, France
- ⁸¹ CNRS-UCB International Research Laboratory, Centre Pierre Binétruy, IRL2007, CPB-IN2P3, Berkeley, USA
- ⁸² University of Applied Sciences and Arts of Northwestern Switzerland, School of Engineering, 5210 Windisch, Switzerland
- ⁸³ Institute of Physics, Laboratory of Astrophysics, Ecole Polytechnique Fédérale de Lausanne (EPFL), Observatoire de Sauverny, 1290 Versoix, Switzerland
- ⁸⁴ Telespazio UK S.L. for European Space Agency (ESA), Camino bajo del Castillo, s/n, Urbanización Villafranca del Castillo, Villanueva de la Cañada, 28692 Madrid, Spain
- ⁸⁵ Institut de Física d'Altes Energies (IFAE), The Barcelona Institute of Science and Technology, Campus UAB, 08193 Bellaterra (Barcelona), Spain
- ⁸⁶ European Space Agency/ESTEC, Keplerlaan 1, 2201 AZ Noordwijk, The Netherlands
- ⁸⁷ DARK, Niels Bohr Institute, University of Copenhagen, Jagtvej 155, 2200 Copenhagen, Denmark
- ⁸⁸ Waterloo Centre for Astrophysics, University of Waterloo, Waterloo, Ontario N2L 3G1, Canada
- ⁸⁹ Department of Physics and Astronomy, University of Waterloo, Waterloo, Ontario N2L 3G1, Canada
- ⁹⁰ Perimeter Institute for Theoretical Physics, Waterloo, Ontario N2L 2Y5, Canada
- ⁹¹ Centre National d'Etudes Spatiales – Centre spatial de Toulouse, 18 avenue Edouard Belin, 31401 Toulouse Cedex 9, France
- ⁹² Institute of Space Science, Str. Atomistilor, nr. 409 Măgurele, Ilfov, 077125, Romania
- ⁹³ Dipartimento di Fisica e Astronomia "G. Galilei", Università di Padova, Via Marzolo 8, 35131 Padova, Italy
- ⁹⁴ INFN-Padova, Via Marzolo 8, 35131 Padova, Italy
- ⁹⁵ Caltech/IPAC, 1200 E. California Blvd., Pasadena, CA 91125, USA
- ⁹⁶ Instituto de Física Teórica UAM-CSIC, Campus de Cantoblanco, 28049 Madrid, Spain
- ⁹⁷ Institut de Recherche en Astrophysique et Planétologie (IRAP), Université de Toulouse, CNRS, UPS, CNES, 14 Av. Edouard Belin, 31400 Toulouse, France
- ⁹⁸ Université St Joseph; Faculty of Sciences, Beirut, Lebanon
- ⁹⁹ Departamento de Física, FCFM, Universidad de Chile, Blanco Encalada 2008, Santiago, Chile
- ¹⁰⁰ Universität Innsbruck, Institut für Astro- und Teilchenphysik, Technikerstr. 25/8, 6020 Innsbruck, Austria
- ¹⁰¹ Department of Physics and Helsinki Institute of Physics, Gustaf Hällströmin katu 2, University of Helsinki, 00014 Helsinki, Finland
- ¹⁰² Centre for Electronic Imaging, Open University, Walton Hall, Milton Keynes, MK7 6AA, UK

- ¹⁰³ Infrared Processing and Analysis Center, California Institute of Technology, Pasadena, CA 91125, USA
- ¹⁰⁴ Departamento de Física, Faculdade de Ciências, Universidade de Lisboa, Edifício C8, Campo Grande, PT1749-016 Lisboa, Portugal
- ¹⁰⁵ Instituto de Astrofísica e Ciências do Espaço, Faculdade de Ciências, Universidade de Lisboa, Tapada da Ajuda, 1349-018 Lisboa, Portugal
- ¹⁰⁶ Cosmic Dawn Center (DAWN)
- ¹⁰⁷ Niels Bohr Institute, University of Copenhagen, Jagtvej 128, 2200 Copenhagen, Denmark
- ¹⁰⁸ Universidad Politécnica de Cartagena, Departamento de Electrónica y Tecnología de Computadoras, Plaza del Hospital 1, 30202 Cartagena, Spain
- ¹⁰⁹ European University of Technology EUT+, European Union
- ¹¹⁰ Institute of Space Sciences (ICE, CSIC), Campus UAB, Carrer de Can Magrans, s/n, 08193 Barcelona, Spain
- ¹¹¹ Institut d'Estudis Espacials de Catalunya (IEEC), Edifici RDIT, Campus UPC, 08860 Castelldefels, Barcelona, Spain
- ¹¹² Kapteyn Astronomical Institute, University of Groningen, PO Box 800, 9700 AV Groningen, The Netherlands
- ¹¹³ Université PSL, Observatoire de Paris, Sorbonne Université, CNRS, LERMA, 75014, Paris, France
- ¹¹⁴ Université Paris-Cité, 5 Rue Thomas Mann, 75013, Paris, France